Journal of Materials Science: Materials in Electronics (2018) 29:7203–7212
https://doi.org/10.1007/s10854-018-8708-x

Luminescence properties and energy transfer of co-doped $Ba_3GdNa(PO_4)_3F:Ce^{3+},Tb^{3+}$ green-emitting phosphors

Zaifa Yang[1] · Yuanxun Yu[1] · Gongnian Zhang[1] · Changjian Ji[1] · Hongxia Bu[1] · Denghui Xu[2] · Jiayue Sun[2]

Received: 12 October 2017 / Accepted: 31 January 2018 / Published online: 1 February 2018

Abstract
Phase pure Ce^{3+} and Tb^{3+} singly doped and Ce^{3+}/Tb^{3+} co-doped $Ba_3GdNa(PO_4)_3F$ samples have been synthesized via the high temperature solid-state reaction. The crystal structures, photoluminescence properties, fluorescence lifetimes, thermal properties and energy transfer of $Ba_3GdNa(PO_4)_3F:Ce^{3+},Tb^{3+}$ were systematically investigated. Rietveld structure refinement indicates that $Ba_3GdNa(PO_4)_3F$ crystallizes in a hexagonal crystal system with the space group *P-6*. For the co-doped $Ba_3GdNa(PO_4)_3F:Ce^{3+},Tb^{3+}$ samples, the emission color can be tuned from blue to green by varying the doping concentration of the Tb^{3+} ions. The intense green emission was realized in the $Ba_3GdNa(PO_4)_3F:Ce^{3+},Tb^{3+}$ phosphors on the basis of the highly efficient energy transfer from Ce^{3+} to Tb^{3+}. Also the energy transfer mechanism has been confirmed to be quadrupole–quadrupole interaction, which can be validated via the agreement of critical distances obtained from the concentration quenching (13.84 Å). These results show that the developed phosphors may possess potential applications in near-ultraviolet pumped white light-emitting diodes.

1 Introduction

In the past decade, more and more interest has been focused on the GaN-based light-emitting diode (LED) technology, especially the developing advanced solid-state lighting sources [1]. The LED-based lighting have gained significant attention over conventional lighting sources due to their advantages such as significant power saving, longer lifetime, higher luminous efficiency, and brightness, etc [2, 3]. Nowadays the commonly used white emitting LEDs are based on the combination of a blue InGaN LED chip and a yellow emitting $Y_3Al_5O_{12}:Ce^{3+}$ (YAG:Ce). However, these systems have a low color rendering index (CRI, $Ra < 80$) and a high color temperature due to the lack of red-emitting component [4]. Therefore, it is crucial to develop the new phosphors with high chemical stability and strong absorption in ultraviolet (UV) or near-ultraviolet (NUV) region with high conversion efficiency [5].

The Tb^{3+} ion, a well-known activator, emits a green color as a result of its main $^5D_4$–$^7F_5$ transition with an emission peak around 545 nm [6]. The absorption peaks of Tb^{3+} in the NUV region above 290 nm are rather weak and narrow because these transitions belong to the 4f–4f forbidden transition. Nevertheless, the Ce^{3+} ion can be used as an important sensitizer for Tb^{3+} ions by transferring part of its excitation energy to Tb^{3+} as a result of its strong 4f–5d absorption in NUV region [7]. As a promising sensitizer for Tb^{3+} ions, Ce^{3+} ions have been extensively applied in many Tb^{3+}-doped hosts, such as $Ba_3Lu(PO_4)_3$, $Sr_2La_8(SiO_4)_6O_2$, and $Sr_3Lu(PO_4)_3$ [8–10]. It was found that Tb^{3+} can be sensitized by Ce^{3+} in these lattices due to the spectral overlap between the emission band of Ce^{3+} and the excitation band of Tb^{3+}. Consequently, the tunable emission from blue to green can be produced in the type of Ce^{3+}/Tb^{3+} co-doped BGNPF single-composition host.

As is well known, an appropriate host matrix is crucial in the generation of white light. Apatite is a structural type for compounds with the general formula $M_{10}(XO_4)_6L_2$ (M = Ca, Sr, Ba; X = P, As, V, Mn, Cr, Si and Ge; L = F, Cl, OH). It has been known since Naray-Szabo determined the structure of $Ca_{10}(PO_4)_6F_2$ in 1930 and was widely studied due to its biological and industrial importance [11, 12]. Recently, a variety of phosphates with the formula BGNPF have been reported in the literatures, such as

✉ Zaifa Yang
fazaiyang@163.com

[1] College of Physics and Electronic Engineering, Qilu Normal University, Jinan 250200, People's Republic of China

[2] School of Science, Beijing Technology and Business University, Beijing 100048, People's Republic of China

$Ba_3NaGd(PO_4)_3F:Eu^{2+}$, $Ba_3KGd(PO_4)_3F:Tb^{3+},Eu^{3+}$, and $Ba_3NaGd(PO_4)_3F:Eu^{2+},Tb^{3+}$ [13–15]. And these results show that the host material BGNPF possess the advantages of low synthetic temperature and high thermal/chemical stability. To the best of our knowledge, the luminescence properties of BGNPF:Ce^{3+},Tb^{3+} have not been investigated yet. We therefore co-doped the rare earth ions Ce^{3+} and Tb^{3+} into the BGNPF host. In the present work, we reported the crystal structure refinement of BGNPF and preferred crystallographic sites for activators. BGNPF crystallizes in a hexagonal unit cell with the space group *P-6* and lattice constants of a = 9.80587 Å, c = 7.33931 Å, and cell volume = 611.164 $Å^3$ based on the powder diffraction Rietveld refinement. Moreover, we have demonstrated a novel blue–green tunable BGNPF:Ce^{3+},Tb^{3+} phosphor by varying the relative ratios of Ce^{3+}/Tb^{3+}. Their detailed luminescence properties and the energy transfer between Ce^{3+} and Tb^{3+} have been discussed, and the energy transfer mechanism between Ce^{3+} and Tb^{3+} ions has been investigated systematically.

2 Experimental

2.1 Materials and synthesis

$BaCO_3$ (A.R. (Analytical Reagent)), BaF_2 (A.R.), Na_2CO_3 (A.R.), $(NH_4)_2HPO_4$ (A.R.), Gd_2O_3 (99.99%), CeO_2 (99.99%), and Tb_4O_7 (99.99%) were employed as the raw materials. In addition, 20% excess of BaF_2 was added to compensate the loss of fluorine. These samples were weighted with designed chemical compositions and thoroughly mixed in an agate mortar for 25 min. Then the mixtures were taken in an alumina crucible and sintered at 1050 °C for 4 h in a corundum crucible imbedded in active carbon. Finally, after natural cooling to room temperature, grounding powder for the following analysis.

2.2 Characterization methods

The X-ray Powder diffraction spectroscopy of the as-prepared phosphor was identified by a Bruker D2 Focus diffractometer with Cu Kα radiation (λ = 1.5406 Å). The morphology of the samples was determined by a field-emission scanning electron microscope (FE-SEM, S-4800, Hitachi, Japan). The photoluminescence (PL) and photoluminescence excitation (PLE) spectra of the samples were obtained using a fluorescence spectrophotometer (F-7000, Hitachi, Japan) equipped with a 150 W Xe lamp used as an excitation source. The luminescence decay curve was obtained using a spectrofluorometer (HORIBA, JOBIN YVON FL3-21) with xenon flash lamp as the source. The temperature-dependence PL spectra were measured on the same spectrophotometer with a self-made heating attachment (Tianjin Orient KOJI Co. Ltd, TAP-02).

3 Results and discussion

3.1 Crystal structures and phase analysis

As a representative, the XRD patterns of BGNPF host, BGNPF:$0.22Ce^{3+}$, BGNPF:$0.16Tb^{3+}$, BGNPF:$0.22Ce^{3+}$,$0.16Tb^{3+}$, and the reference diffraction lines based on the JCPDS card with no. 71-1317 are shown in Fig. 1. The results of XRD analysis confirm that the XRD patterns of all the samples are in good agreement with the reported BGNPF phase without any impurity phase. This fact suggests that Ce^{3+} and Tb^{3+} ions have been successfully built into the BGNPF host lattice and do not destroy the lattice structure of BGNPF host. The inset of Fig. 1 represents the SEM micrograph of the BGNPF:$0.22Ce^{3+}$,$0.16Tb^{3+}$ phosphors. It can be seen that the obtained powders consist of particles with size around several microns which usually occurs in the high temperature solid state reaction. Meantime, it is clear that the sizes of the BGNPF:$0.22Ce^{3+}$,$0.16Tb^{3+}$ aggregations are in the range of 1–6 μm. This is a suitable size for fabrication of solid-state lighting devices [16].

To further understand the crystal structure of BGNPF, Fig. 2 presents the experimental, calculated, background and difference results of the XRD profiles for the Rietveld refinement of BGNPF host and the corresponding refined parameters are listed in in Table 1. Rietveld refinement was performed using General Structure Analysis System

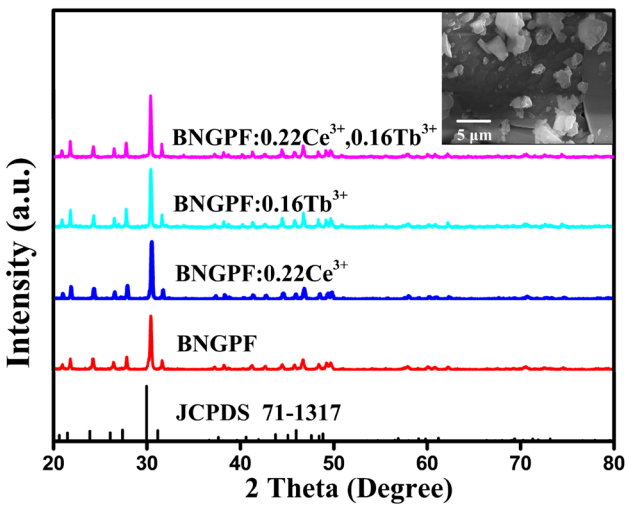

Fig. 1 The XRD patterns of BGNPF host, BGNPF:$0.22Ce^{3+}$, BGNPF:$0.16Tb^{3+}$, BGNPF:$0.22Ce^{3+}$,$0.16Tb^{3+}$ samples and the standard pattern of JCPDS card file of 71-1317. Inset: the SEM micrograph of BGNPF:$0.22Ce^{3+}$,$0.16Tb^{3+}$ phosphor

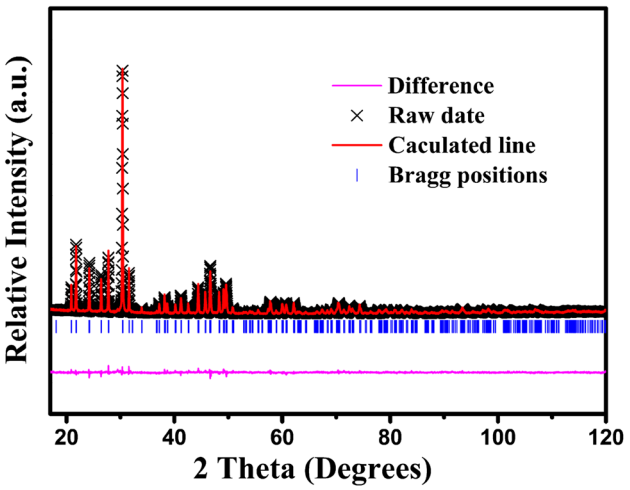

Fig. 2 Rietveld refinement of the XRD profile of BGNPF

(GSAS) software, and it was found that almost all peaks were indexed to a hexagonal cell with parameters close to those of the BGNPF phase [17]. The phosphor was found to crystallize in the hexagonal crystal system with the space group of *P-6* and its cell parameters were a = b = 9.80587 Å, c = 7.33931 Å and V = 611.164 Å^3. The refinement finally converged to $R_p = 3.8\%$, $R_{wp} = 4.89\%$, and $\chi^2 = 1.84$, indicating that all the observed peaks satisfy the reflection conditions and our prepared phosphor is of single phase.

Furthermore, Fig. 3a, b show the unit cell structure of BGNPF sample viewed from the c axis. In the host, the cations are connected by the $[PO_4]^{3-}$ tetrahedral formed by the P and O atoms. In this crystal structure, there exist two kinds of Gd^{3+} ions sites, which are named Gd1 and Gd2 here for identification. Gd1 is coordinated by two fluorine atoms and five oxygen atoms; Gd2 is coordinated by nine oxygen atoms. The coordination environment around the four cationic sites Gd1 and Gd2 are given in Fig. 3c. Compared with the ionic radii and valence state, the doped Ce^{3+} ions (r = 0.102 nm) and Tb^{3+} (r = 0.092 nm) are easy to substitute the Gd^{3+} (r = 0.094 nm) ions [18].

3.2 Luminescent properties of Ce^{3+}, Tb^{3+} and Ce^{3+}/Tb^{3+} co-doped in BGNPF

The PL as well as PLE spectra of BGNPF:0.22Ce^{3+} are depicted in Fig. 4a. The PLE spectrum consists of three absorption bands that peaking at about 224, 273 and 314 nm, which correspond to the transitions from the ground state of the Ce^{3+} ions to the field splitting levels of the 5d state [19]. Upon the excitation of 273 nm, the PL spectrum shows an asymmetric broad band peaking at 351 nm. The asymmetric emission band can be decomposed into two Gaussian bands (dash lines) peaking at 362 and 379 nm, which correspond to the Gd1/Gd2 independent sites. The energy difference is close to the energy separation between the $^2F_{7/2}$ and $^2F_{5/2}$ levels [20]. Figure 4b shows the PL spectra of BGNPF:$x$$Ce^{3+}$ (x = 0.03, 0.06, 0.09, 0.12, 0.18, 0.22, 0.24, 0.26, 0.30 and 0.32). The PL intensity of Ce^{3+} increases with its increasing concentration (x) and the intensity reaches a maximum value at $x = 0.22$. However, when above the optimal Ce^{3+} amount, the emission intensity is found to decline because of the concentration quenching effect.

According to the theory of Blasse, the concentration quenching among the same activator ions is mainly ascribed to the non-radiative energy migration. The critical distance (R_c) can be calculated by the following equation [21]:

$$R_c \approx 2\left[\frac{3V}{4\pi x_c N}\right] \quad (1)$$

Table 1 Rietveld refinement results and crystal data for the BGNPF host

Atom	X	Y	Z	Wyckoff position	Occupancy	Mult.
P	0.04074	0.40915	0.23900	6g	1	6
Ba1	0.25010	0.22839	0.25656	6g	0.899	6
Ba2	0.25010	0.22839	0.25656	6g	0.048	6
Ba3	0.25010	0.22839	0.25656	6g	0.038	6
Gd1	0.33333	0.66667	0.01313	2d	0.343	2
Na1	0.33333	0.66667	0.01313	2d	0.069	2
Gd2	0.33333	0.66667	0.48453	2d	0.259	2
Na2	0.33333	0.66667	0.48453	2d	0.070	2
O1	0.52033	0.17404	0.20600	6g	1	6
O2	0.04654	0.31633	0.40919	6g	1	6
O3	0.06592	0.41960	0.02659	6g	1	6
O4	0.15988	0.61464	0.30500	6g	1	6
F	0	0	0.05074	2d	1	2

Space group: *P6*—hexagonal; a = 6 = 9.80587 Å, c = 7.33931 Å, V = 611.164Å^3, 2θ-interval = 10–120°, R_{wp} (%) = 4.89, R_p (%) = 3.80, $\chi^2 = 1.84$

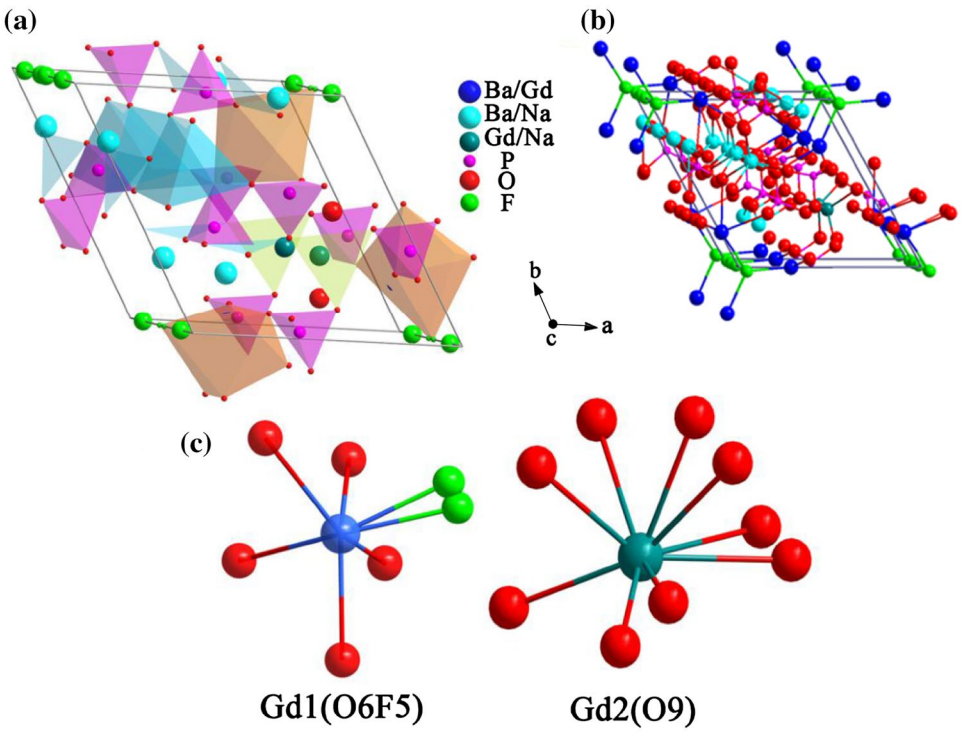

Fig. 3 Schematic illustration of the crystal structure of BGNPF viewed from the c axis, and the coordination environment around Gd1 and Gd2

where V is the volume of one unit cell, x_c is the critical concentration and N is the number of the cationic sites occupied by activators in one unit cell. For BGNPF host, V = 611.164 Å^3, N = 2, x_c = 0.22. As a result, the critical distance of energy transfer can be quickly obtained to be 13.84 Å by using Eq. (1). Based on the theory of Van Uitert, if the critical distance between the sensitizer and activator is shorter than 5 Å, the exchange interaction is dominant in the process of energy transfer [22]. Therefore the electric multipolar interaction will take place for quenching mechanism in Ce^{3+} doped samples. According to the energy transfer theory of Van Uiter, the relationship between the luminescent intensity (I) and the doping concentration (x) follows the equation [23]:

$$\frac{I}{x} = K\left(1 + \beta(x)^{Q/3}\right)^{-1} \tag{2}$$

where I is the integral intensity of emission spectra, x is the activator concentration beyond the optimal concentration, K and β are constants, Q represents the interaction type between rare earth ions, here Q = 6, 8 or 10, indicating the dipole–dipole, dipole–quadrupole or quadrupole–quadrupole interaction, respectively. As shown in Fig. 5, the relation between log (I/x) and log (x) is found to be an approximately linear and the slope is about − 2.86. The value of Q, thus, turns out to 8.58, which is approximately equal to 8. This indicates that the dipole–quadrupole interaction is the major mechanism for concentration quenching in BGNPF:$x$$Ce^{3+}$ phosphors.

The excitation and emission spectra of BGNPF:0.22Ce^{3+} and BGNPF:0.16Tb^{3+} samples are shown in Fig. 6a, b, respectively. The excitation spectrum monitored at 545 nm for BGNPF:0.16Tb^{3+} sample exhibits a shoulder and a broad band centered at 223 and 276 nm, which correspond to the spin-allowed $4f^8$–$4f^75d^1$ ($^7F_6$–^7D) and spin-forbidden $4f^8$–$4f^75d$ ($^7F_6$–^9D) transition of Tb^{3+} ions [24]. When the sample is excited at 276 nm, the emission spectrum exhibits four sharp peaks located at 489, 545, 589 and 624 nm which are assigned to the $^5D_4$–^7F_J (J = 6, 5, 4 and 3) ascribed to the characteristic transition of Tb^{3+}, respectively [25]. The phosphor exhibits green emitting hue due to the maximum peak at 545 nm. The PLE and PL spectra of the BGNPF:0.22Ce^{3+},0.16Tb^{3+} phosphor are shown in Fig. 6c. At the irradiation of 273 nm, the PL spectrum exhibits both the Ce^{3+} and the typical Tb^{3+} emissions. In addition, to avoid the existence of the Ce^{3+} emission, we chose the emission peak at 545 nm as monitoring wavelength which is beyond the emission range of the Ce^{3+} ions. From Fig. 6c, we can see that the PLE spectrum is similar to that monitored at 351 nm. So the energy transfer from Ce^{3+} to Tb^{3+} ions can be achieved in the BGNPF system. To further confirm the phenomenon, Fig. 6d illustrates the PL spectra of BGNPF:0.22Ce^{3+} and PLE spectra of BGNPF:0.16Tb^{3+} phosphors. A notable spectral overlap between the PL spectrum of BGNPF:0.22Ce^{3+} and the PLE spectrum of BGNPF:0.16Tb^{3+} is observed. The above analysis on the PL and PLE spectra of the phosphors proves the occurrence of the energy transfer from the Ce^{3+} to Tb^{3+} ions [26].

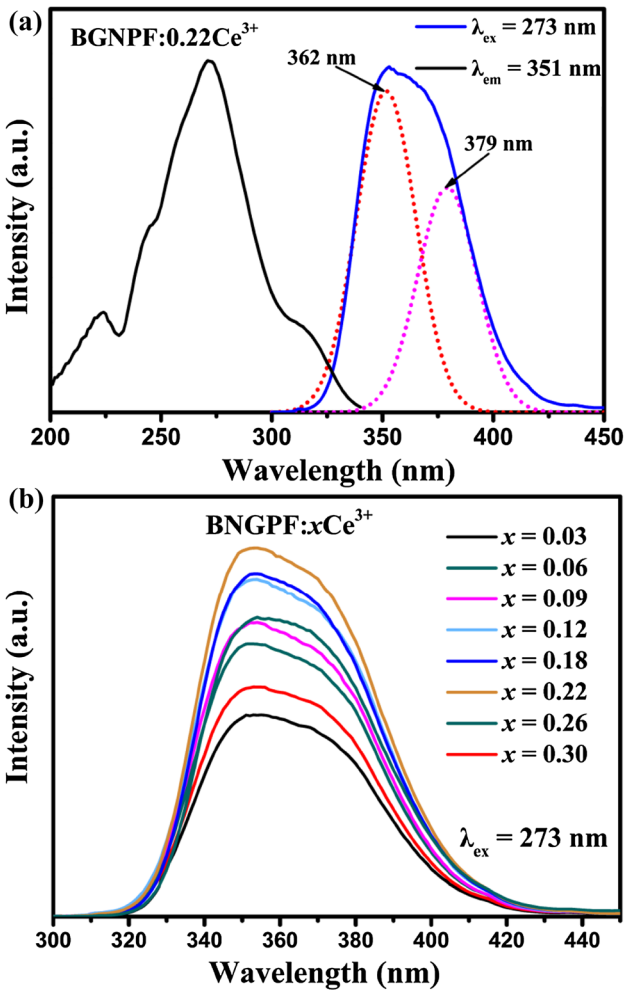

Fig. 4 **a** PLE and PE spectra of BGNPF:0.22Ce^{3+}; **b** PL spectra of BGNPF:xCe^{3+} (x = 0.03, 0.06, 0.09, 0.12, 0.18, 0.22, 0.26, 0.30)

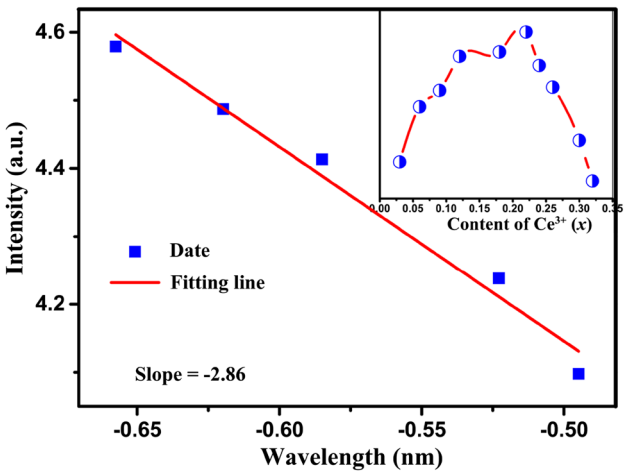

Fig. 5 The relationship of log(x) versus log(I/x) for BGNPF:xCe^{3+} (x = 0.22, 0.24, 0.26, 0.30, 0.32) phosphor; the inset shows the variation of emission intensity as a function of doped Ce^{3+} molar concentration

3.3 Energy transfer of Ce^{3+}/Tb^{3+} co-doped BGNPF phosphors

As mentioned above, energy transfer can be expected from the spectral overlap of the singly doped samples. In order to investigate the energy transfer process in the BGNPF host lattice, the fluorescence decay curves of Ce^{3+} with different Tb^{3+} doping contents are illustrated in Fig. 7a. According to the decay behavior of Ce^{3+}, their corresponding luminescence decay curves can be best fitted with a typical second-order exponential c the following equation [27]:

$$I(t) = A_1 \exp\left(-t/t_1\right) + A_2 \exp\left(-t/t_2\right) \quad (3)$$

where I is the luminescence intensity at time t, A_1 and A_2 are constants, t is the time, and t_1 and t_2 are the decay time for the exponential components. Then, the average decay lifetime τ can be calculated as follows:

$$\tau = \frac{A_1 t_1^{\,2} + A_2 t_2^{\,2}}{A_1 t_1 + A_2 t_2} \quad (4)$$

According to the Eq. (4), and decay curve fitting date in Fig. 7a, the average decay lifetimes τ are calculated to be 37.35, 32.41, 27.50, 24.93, 19.32 and 7.6 ns for BGNPF:0.22Ce^{3+},yTb^{3+} with y = 0, 0.04, 0.08, 0.12, 0.16 and 0.24, respectively. These phenomena strongly demonstrated the energy transfer from Ce^{3+} to Tb^{3+}. In addition, the energy transfer efficiency η between the Ce^{3+} and Tb^{3+} ions can be obtained from the following equation [28]:

$$\eta_T = 1 - \tau/\tau_0 \quad (5)$$

where τ and τ_0 are the decay times of the sensitizer Ce^{3+} in the presence and absence of the activator Tb^{3+}, respectively. As shown in Fig. 7b, the energy transfer efficiencies increase gradually with increasing Tb^{3+} concentration. The value of η_T reaches the maximum of 80% for the emission center monitored at 545 nm when y = 0.24, indicating that the energy transfer from the Ce^{3+} to Tb^{3+} is efficient.

To further analyze the energy transfer behaviors from Ce^{3+} to Tb^{3+}, Fig. 8 illustrates a series of emission spectra for BGNPF:0.22Ce^{3+},yTb^{3+} (y = 0, 0.04, 0.08, 0.12, 0.16, 0.24) excited at 273 nm. With increasing Tb^{3+} concentration, it is found that the emission colors of this series of phosphors varied from blue to green. In addition, one can see that the emission intensity of Ce^{3+} ions decreased monotonously with the increasing Tb^{3+} content in the insert of Fig. 8. Conversely, the emission intensity of the Tb^{3+} ions increased greatly as y changed from 0 to 0.24. These results reflect the behaviors of the energy transfer from Ce^{3+} to Tb^{3+}.

According to Dexter's energy transfer formula for exchange and multipolar interactions and Reisfeld's approximation, the following relation can be acquired [29]:

$$\left(I_{s0}/I_s\right) \propto C^{n/3} \quad (6)$$

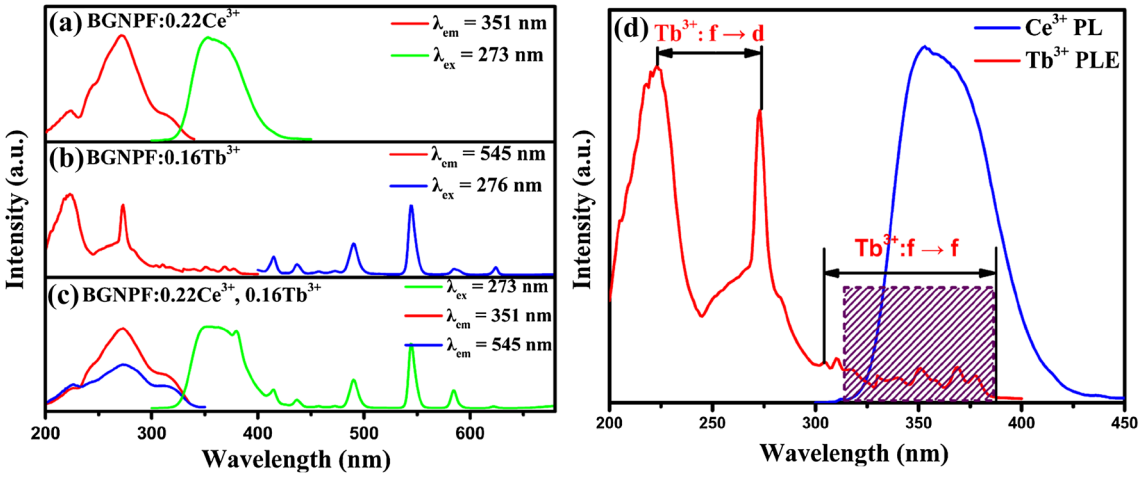

Fig. 6 PLE and PL spectra of **a** BGNPF:0.22Ce^{3+}, **b** BGNPF:0.16Tb^{3+}, and **c** BGNPF:0.22Ce^{3+},0.16Tb^{3+} phosphors; **d** PLE spectra of BGNPF:0.16Tb^{3+} and PL spectra of BGNPF:0.22Ce^{3+} phosphors

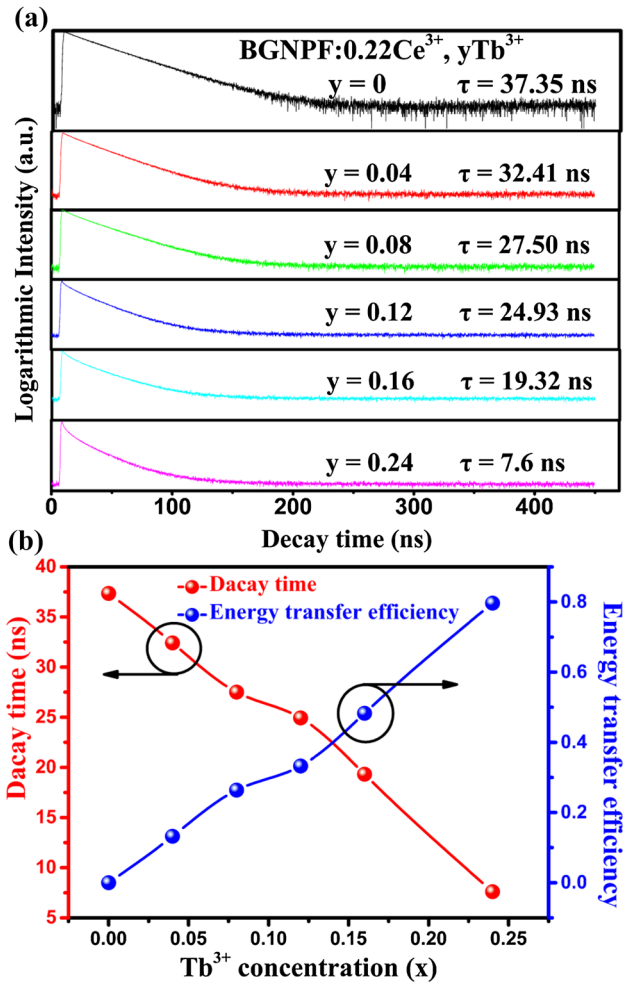

Fig. 7 **a** Decay curves of Ce^{3+} emission monitored at 351 nm for BGNPF:0.22Ce^{3+},yTb^{3+} (y = 0, 0.04, 0.08, 0.12, 0.16, 0.24). **b** The fluorescence lifetime of Ce^{3+} ions and energy transfer efficiencies from Ce^{3+} to Tb^{3+} as a function of Tb^{3+} concentration

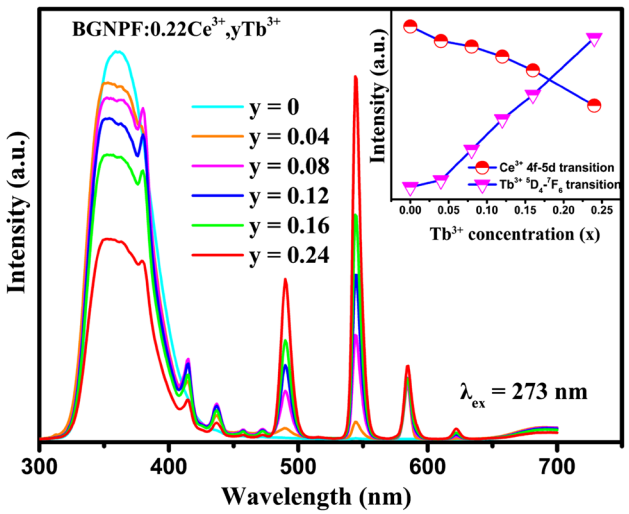

Fig. 8 PL spectra of BGNPF:0.22Ce^{3+},yTb^{3+} (y = 0, 0.04, 0.08, 0.12, 0.16, 0.24) phosphors; the inset shows relative emission intensity of Ce^{3+} and Tb^{3+} in BGNPF:0.22Ce^{3+},yTb^{3+} phosphor

where I_{S0} and I_S are emission intensity of Ce^{3+} in the absence and presence of Tb^{3+}, respectively. C is the total doping concentration of the Ce^{3+} and Tb^{3+} ions. The relationship of $I_{S0}/I_S \propto C^{n/3}$ corresponds to the exchange interaction, and n = 6, 8, and 10 are ascribed to dipole–dipole, dipole–quadrupole, and quadrupole–quadrupole interactions. The plots of $(I_{S0}/I_S) - C^{n/3}$ are illustrated in Fig. 9a–c. The linear relationship reaches the optimal one for $I_{S0}/I_S \propto C^{n/3}$ by comparing the fitting factors of R^2 values in Fig. 9c, implying that energy transfer from Ce^{3+} to Tb^{3+} occurs via the quadrupole–quadrupole interaction.

In an effort to understand the energy transfer process, Fig. 10 shows the energy level model for energy transfer

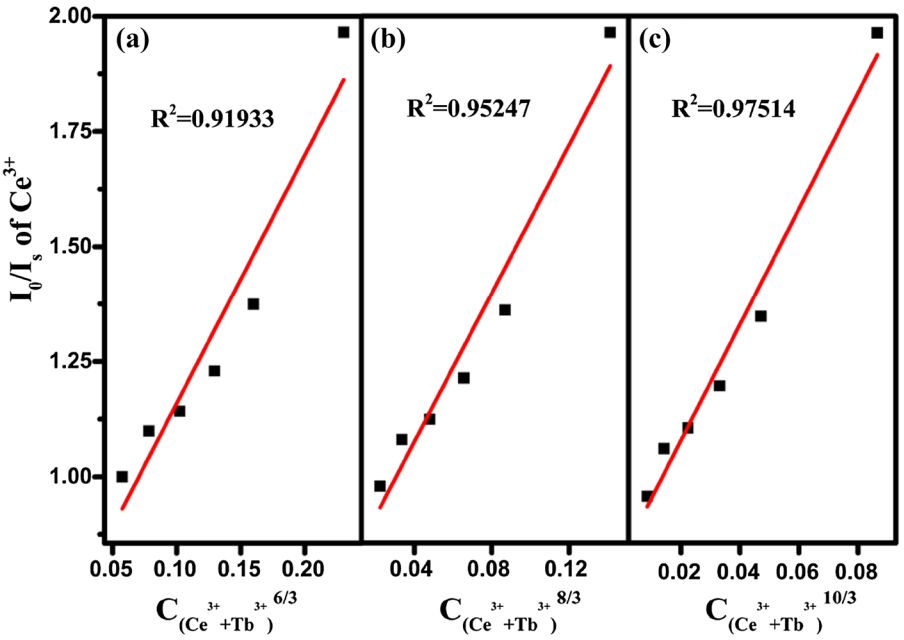

Fig. 9 Dependence of I_{S0}/I_S of Ce^{3+} on **a** $C^{6/3}$, **b** $C^{8/3}$, and **c** $C^{10/3}$

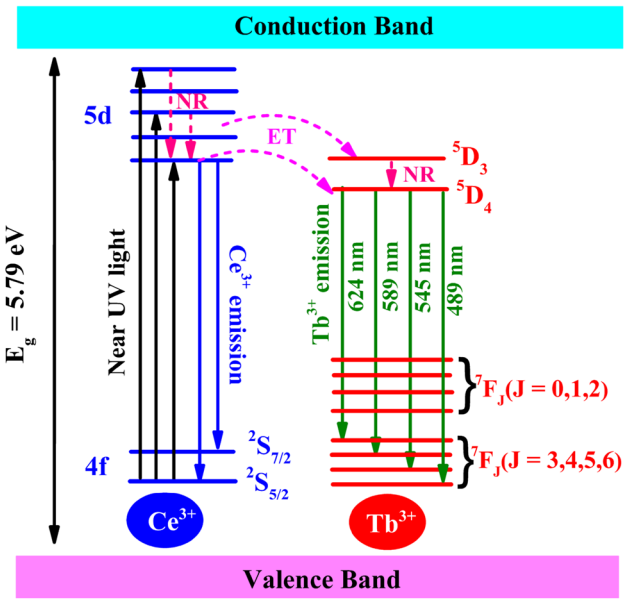

Fig. 10 The schematic of energy transfer in BGNPF:Ce^{3+},Tb^{3+}

process of $Ce^{3+} \rightarrow Tb^{3+}$. When excited at 273 nm, the excited electrons shift to the excited state ($4f^{6}5d$) of Ce^{3+} and non-radiatively (NR) relaxes to the lowest 5d crystal field splitting state, and then the electrons of the Ce^{3+} ions shift from the excited state ($4f^{6}5d$) to its ground state at $^2F_{5/2}$ and $^2F_{7/2}$ levels with a consequent broad band emission. Subsequently, some decay to the $^2F_{5/2}$ and $^2F_{7/2}$ levels occurs via a radiative process. As a consequence of the matched energy levels of Ce^{3+} and Tb^{3+}, other photons transfer the excitation energy to the high excited levels of Tb^{3+} ($4f^{n}$). Finally, the $^5D_4$ level gives the strong emission of Tb^{3+} ($^5D_4 \rightarrow {}^7F_J$, J = 3, 4, 5 and 6) [30].

3.4 CIE chromaticity coordinates and thermal stability of BGNPF:Ce^{3+},Tb^{3+}

The x and y values of the Commission Internationale de L'Eclairage (CIE) chromaticity coordinates for different samples in BGNPF:0.22Ce^{3+},yTb^{3+} phosphors were measured based on the corresponding PL spectra upon 273 nm excitation, and the results are summarized in Fig. 11 and Table 2, respectively. From the luminescence photographs of the samples in Fig. 11, it can be seen that the colour tone of the phosphors can be easily modulated from blue (0.252, 0.133) to green (0.290, 0.507) with an increase in the doping content with Tb^{3+}, confirming that the CIE chromaticity coordinates are tunable. Based on these findings, it is clear that these bluish green BGNPF:Ce^{3+},Tb^{3+} phosphors can be efficiently excited in the NUV range. This suggests that BGNPF:Ce^{3+},Tb^{3+} can act as a promising bluish green tunable phosphor for possible applications in solid-state lighting and displays [31].

In general, the thermal stability of luminescence intensity of phosphors has a great significance for the practical application of w-LEDs [32]. Figure 12a showed the relative emission intensities of the BGNPF:0.22Ce^{3+},0.16Tb^{3+} phosphor measured under 273 nm excitation and Fig. 12b presented the detailed tendency to decrease for the emission intensities under different temperatures. From the Fig. 12a, b, we can see the PL intensities just decreased to 94% of the initial intensity (50 °C) at 150 °C. That shows its excellent temperature stability of the BGNPF:0.22Ce^{3+},0.16Tb^{3+} phosphor. Generally, the decrease

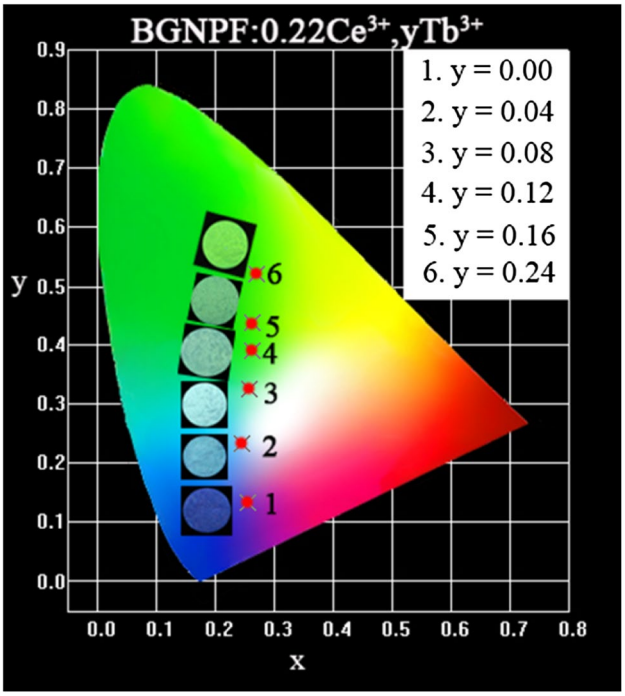

Fig. 11 CIE chromaticity coordinates and the luminescence photographs of BGNPF:0.22Ce^{3+},yTb^{3+} (y = 0, 0.04, 0.08, 0.12, 0.16 and 0.24) under excitation at 273 nm

Table 2 Comparison of CIE chromaticity coordinates for BGNPF:Ce^{3+},nTb^{3+} phosphors

Sample no.	Sample composition (n)	CIE coordinates (x, y)
1	0	(0.252, 0.133)
2	0.04	(0.246, 0.238)
3	0.08	(0.261, 0.317)
4	0.12	(0.277, 0.391)
5	0.16	(0.283, 0.424)
6	0.22	(0.290, 0.507)

of emission intensity is ascribed to the thermal quenching of emission intensity via phonon interaction. And the configuration coordinate diagram as shown in Fig. 12c can be used to explain the temperature quenching mechanism [33]. With the increase in temperature, electrons at lower excited levels C could jump to higher excited levels E, assisted by thermal phonons. Electrons at state E can go back to the 4f ground state A in a non-radiative way, making the number of electrons which can go back to the ground state through radiation decrease.

Furthermore, the activation energy from the thermal quenching can be calculated using the Arrhenius equation [34]:

$$I(T) = \frac{I_o}{1 + c\exp\left(-(\Delta E/KT)\right)} \tag{7}$$

where I_0 is the initial intensity, $I(T)$ is the intensity at a given temperature T, ΔE is the activation energy for thermal quenching, c is a constant for a certain host, and K is the Boltzmann constant (8.629×10^{-5} eV). And, the plot of $\ln[(I_0/I_T)-1]$ versus 1/(kT) are shown in Fig. 12d. The activation energy (ΔE) was deduced to be 3.22 eV by the fitting process, which is much higher than commercial phosphor YAG:Ce^{3+} ($\Delta E = 0.136$ eV). It can be concluded that the relatively high activation energy ΔE resulting in the excellent thermal stability of our phosphors.

In general, for the practical application of phosphors for LEDs, the quantum efficiency (QE) of the phosphor is an important factor to be considered. We have also measured the internal QE of BGNPF:0.22Ce^{3+},yTb^{3+} phosphor according to the reported method [35, 36]. The internal QE value can be calculated by Eq. (8):

$$\eta_{QE} = \frac{\int L_S}{\int E_R - \int E_S} \tag{8}$$

where L_S is the luminescence emission spectrum of the sample; E_S is the spectrum of the light used for exciting the sample; E_R is the spectrum of the excitation light without the sample in the sphere; and all the spectra were collected using the sphere on the FL3-21 fluorescence spectrophotometer. Under the excitation of 273 nm, the recorded quantum yield values of BGNPF:0.22Ce^{3+},yTb^{3+} are 35.9, 42.4, 49.7, 56, and 65.5%, for y = 0.04, 0.08, 0.12, 0.16, and 0.24 respectively, and it is found that the value increases with increasing Tb^{3+} content. These results indicate that BGNPF:0.22Ce^{3+},yTb^{3+} phosphors can act as potential blue–green tunable phosphors for the possible applications in w-LEDs.

4 Conclusions

In summary, a blue and green double-color emitting phosphor BGNPF:Ce^{3+},Tb^{3+} phosphor was successfully prepared by the solid-state reaction. The phase purity, PL properties, energy transfer mechanism, thermal stability and chromaticity coordinates were investigated. The BGNPF:Ce^{3+},Tb^{3+} phosphor shows both a blue emission (351 nm) from Ce^{3+} and a green emission (545 nm) from Tb^{3+} with considerable intensity under NUV excitation. The energy transfer from Ce^{3+} to Tb^{3+} ions takes place in the BGNPF:Ce^{3+},Tb^{3+} phosphor on the basis of the analysis of the luminescence spectra. The energy transfer mechanism from Ce^{3+} to Tb^{3+} ions was proved to be quadrupole–quadrupole interaction. The energy transfer from Ce^{3+} to Tb^{3+} in the phosphor is also demonstrated by luminescence spectra and lifetime values. This indicates that BGNPF:Ce^{3+},Tb^{3+} can act as

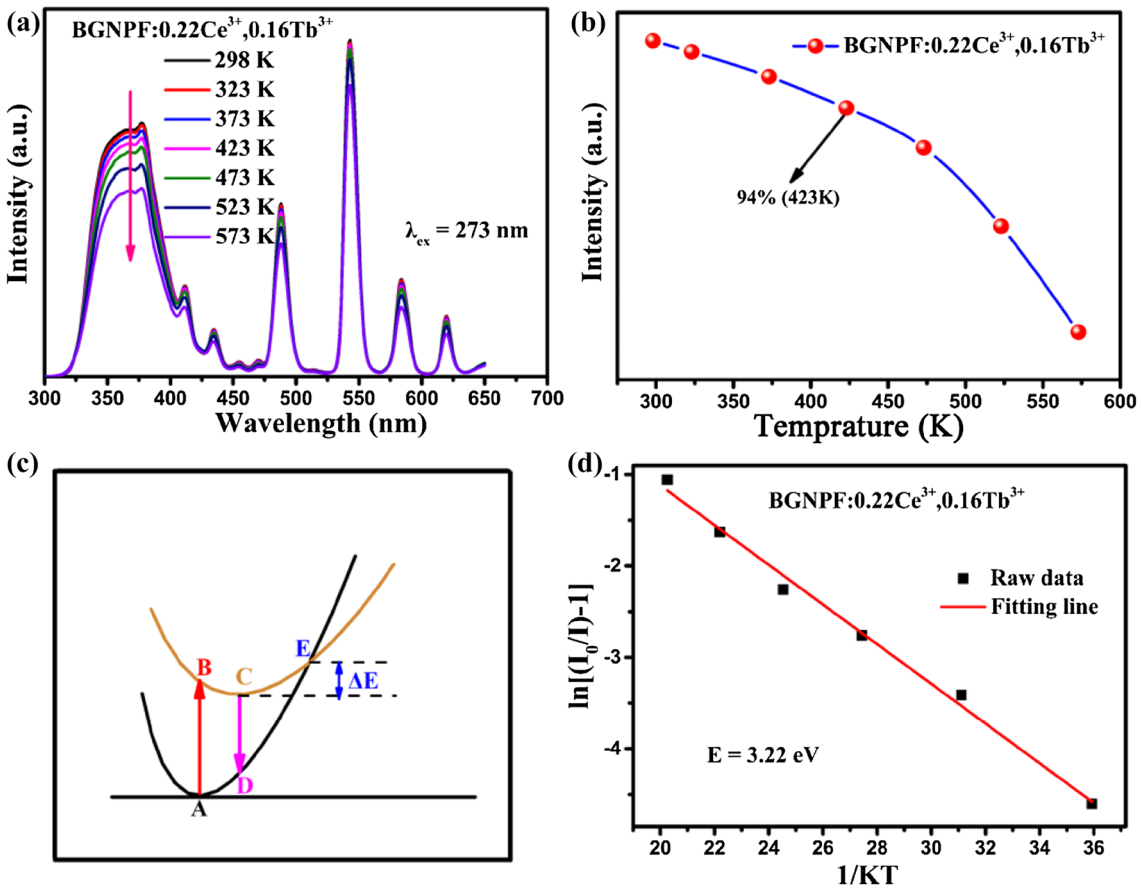

Fig. 12 **a** The temperature-dependent PL spectra of the BGNPF:0.22Ce^{3+},0.16Tb^{3+} under the 273 nm excitation; **b** normalized intensity as a function of temperature; **c** the schematic configuration coordinate diagram for the explanation of temperature quenching; and **d** the plots of $\ln[(I_0/I_T)-1]$ versus 1/kT and the thermal activation energy

a potential blue–green tunable phosphor for application in white LEDs.

Acknowledgements This work was supported by National Natural Science Foundation of China (No. 21576002), National Natural Science Foundation of China (No. 11604170), Natural Science Foundation of Shandong Province, China (No. ZR2014AQ018), Scientific Research in Universities of Shandong Province (No. J16LJ06).

References

1. Z.G. Xia, D.M. Chen, J. Am. Ceram. Soc. **93**, 1397 (2010)
2. C. Yue, W.R. Wang, Q.Q. Wang, Y. Jin, Ceram. J. Alloy. Compd. **683**, 575 (2016)
3. Z.F. Yang, Y.M. Sun, Q.G. Xu, J.Y. Sun, J. Rare Earths **33**, 1251 (2015)
4. Z.G. Xia, Z.H. Xu, M.Y. Chen, Q.L. Liu, Dalton Trans. **45**, 11214 (2016)
5. W.L. Guo, Y. Tian, P. Huang, L. Wang, Q.F. Shi, C.E. Cui, Ceram. Int. **42**, 5427 (2016)
6. Z.G. Xia, Q.L. Liu, Prog. Mater. Sci. **84**, 59 (2016)
7. C.H. Hsu, C.H. Lu, J. Mater. Chem. **21**, 2932 (2011)
8. C. Jin, H.X. Ma, Y.F. Liu, Q.B. Liu, G.Y. Dong, Q.M. Yu, J. Alloy. Compd. **613**, 275 (2014)
9. Q.F. Guo, L.B. Liao, L.F. Mei, H.K. Liu, Y. Hai, J. Solid State Chem. **225**, 149 (2015)
10. Z.F. Yang, D.H. Xu, J.Y. Sun, J.N. Du, X.D. Gao, Mater. Sci. Eng. B **211**, 13 (2016)
11. I. Mayer, R. Roth, W. Brown, J. Solid State Chem. **11**, 33 (1974)
12. M. Xie, R. Pan, Opt. Mater. **35**, 1162 (2013)
13. C.X. Li, J. Dai, J. Huang, D.G. Deng, H. Yu, L. Wang, Y.T. Ma, Y.J. Hua, S.Q. Xu, Ceram. Int. **42**, 6891 (2016)
14. C. Zeng, Y.M. Hu, Z.G. Xia, H.W. Huang, RSC Adv. **5**, 68099 (2015)
15. C. Zeng, H.K. Liu, Y.M. Hun, L.B. Liao, L.F. Mei, Opt. Laser Technol. **74**, 6 (2015)
16. Z.W. Zhang, C.L. Han, W.W. Shi, Y.Y. Kang, Y.S. Wang, W.G. Zhang, D.J. Wang, J. Mater. Sci. Mater. Electron. **26**, 1923 (2015)
17. B.H. Toby, J. Appl. Crystallogr. **34**, 210 (2001)
18. Y. Jin, Q.P. Wang, H.P. Zhou, L.L. Zhang, J.H. Zhang, Ceram. Int. **42**, 3309 (2016)
19. H. Xu, Z.G. Xia, H.K. Liu, L.B. Liao, ECS J. Solid State Technol. **2**, 186 (2013)
20. W.W. Holloway Jr., M. Kestigian, J. Opt. Soc. Am. **59**, 60 (1969)
21. G. Blasse, Philips Res. Rep. **24**, 131 (1969)
22. R. Chen, Y.H. Hu, Y.H. Jin, L. Chen, X.J. Wang, Appl. Phys. A **117**, 823 (2014)
23. L.G. Van Uitert, J. Electrochem. Soc. **114**, 1048 (1967)

24. Q.H. Zhang, H.Y. Ni, L.L. Wang, F.M. Xiao, Ceram. Int. **42**, 6115 (2016)
25. H.H. Lin, G.B. Zhang, P.A. Tanner, H.B. Liang, J. Phys. Chem. C **117**, 12769 (2013)
26. F.G. Meng, H.Z. Zhang, C.L. Chen, S.I. Kim, H.J. Seo, X.M. Zhang, J. Alloy. Compd. **671**, 150 (2016)
27. R. Pang, C. Li, L. Shi, Q. Su, J. Phys. Chem. Solids **70**, 303 (2009)
28. G. Blasse, Phys. Lett. A **28**, 444 (1968)
29. D.L. Dexter, J.H. Schulman, J. Chem. Phys. **22**, 1063 (1954)
30. Z.G. Xia, R.S. Liu, J. Phys. Chem. C **116**, 15604 (2012)
31. D.H. Xu, Z.F. Yang, J.Y. Sun, X.D. Gao, J.N. Du, J. Mater. Sci. Mater. Electron. **27**, 8370 (2016)
32. W.R. Liu, C.H. Huang, C.W. Yeh, J.C. Tsai, Y.C. Chiu, Y.T. Yeh, R.S. Liu, Inorg. Chem. **51**, 9636 (2012)
33. J.Y. Sun, D.P. Cui, J. Am. Ceram. Soc. **97**, 843 (2014)
34. S. Bhushan, M.V. Chukichev, J. Mater. Sci. Lett. **9**, 319 (1988)
35. Y.S. Xu, X.H. Zhang, S.X. Dai, B. Fan, H.L. Ma, J.L. Adam, J. Ren, G.R. Chen, J. Phys. Chem. C **115**, 13056 (2011)
36. M. Zhao, Z.G. Xia, M.S. Molokeev, L. Ning, Q.L. Liu, Chem. Mater. **29**, 6552 (2017)